Interpretable data-driven turbulence modeling for separated flows using symbolic regression with unit constraints

Boqian Zhang[1] and Juanmian Lei[1, a)]

[1] School of Aerospace Engineering, Beijing Institute of Technology, Beijing, 100081, China

Machine learning techniques have been applied to enhance turbulence modeling in recent years. However, the "black box" nature of most machine learning techniques poses significant interpretability challenges in improving turbulence models. This paper introduces a novel unit-constrained turbulence modeling framework using symbolic regression to overcome these challenges. The framework amends the constitutive equation of linear eddy viscosity models (LEVMs) by establishing explicit equations between the Reynolds stress deviation and mean flow quantities, thereby improving the LEVM model's predictive capability for large separated turbulence. Unit consistency constraints are applied to the symbolic expressions to ensure physical realizability. The framework's effectiveness is demonstrated through its application to the separated flow over 2D periodic hills. Numerical simulations are conducted to validate the accuracy and generalization capabilities of the learned turbulence model. Compared to the standard k-ε model, the learned model exhibits significantly enhanced predictive accuracy for anisotropic Reynolds stresses and flow velocities. It also more accurately identifies flow separations and exhibits promising generalization capabilities across different flow geometries.

I. INTRODUCTION

Turbulence is prevalent across natural phenomena and engineering applications, and Computational Fluid Dynamics (CFD) is an essential tool for studying turbulence. Achieving accurate and efficient numerical simulations of turbulent flows is a significant issue that persists in both academic and industrial spheres. Over the past few decades, a variety of numerical simulation techniques for turbulence have been developed, including Direct Numerical Simulation (DNS), Large Eddy Simulation (LES), and Reynolds-Averaged Navier-Stokes (RANS) approaches, with RANS being the most extensively researched and applied. Despite earlier predictions suggesting that LES might supplant RANS in industrial applications within the forthcoming decades[1], such optimistic expectations have been shattered with the end of "Moore's Law". At least in the near future, RANS will continue to be the primary tool for industrial CFD applications[1,2].

[a)] E-mail: leijm@bit.edu.cn

The RANS method employs the Reynolds-averaged Navier–Stokes equations as the governing equations. A significant challenge within these equations is the non-closed Reynolds stress term, necessitating the development of constitutive equations to elucidate the relationship between the Reynolds stress and the time-averaged flow field variables, thereby achieving closure of the equations. This requirement has led to the creation of various turbulence closure models. Among these, linear eddy viscosity models (LEVMs), based on the Boussinesq assumption, are distinguished by their low computational demands and robust performance, making them a popular choice in engineering applications[3]. The Boussinesq assumption posits a linear relationship between the anisotropic Reynolds stress tensor and the time-averaged flow strain rate tensor. However, this assumption has been proven to diverge from reality in most real-world flows[4], especially in flows with large separation, secondary flows, and curvature, etc., thereby undermining the accuracy of LEVMs in simulating such flows[5]. In contrast to LEVMs, the Reynolds stress model (RSM) and the algebraic stress model (ASM), grounded in the Reynolds stress transport equation, do not rely on the Boussinesq assumption and offer enhanced predictive accuracy for complex turbulence. However, their application has been limited by numerical instability and elevated computational costs[6].

With the advancements in machine learning technologies and the increasing availability of high-precision turbulence data, data-driven turbulence modeling that integrates data with physical prior has emerged as a novel paradigm in turbulence modeling. This paradigm has been successfully applied to enhance LEVMs. Duraisamy et al.[7,8] proposed a turbulence modeling method based on field inversion and machine learning (FIML). They first obtain the spatial distribution of model correction function through field inversion, then use machine learning to establish the mapping relationship between flow variables and the correction parameter, thereby enhancing the turbulence model's predictive capabilities. Ling et al.[9] developed a tensor basis neural network (TBNN) incorporating Galilean invariance to predict the anisotropic Reynolds stress tensor accurately. Wang et al.[2] established the mapping relationship between the mean flow variables and the Reynolds stress tensor based on random forest method, improving the original turbulence model's prediction accuracy for fully developed turbulence in square pipe and large separated flows. Wu et al.[10] further established a comprehensive physics-informed m machine learning framework for turbulence modeling, addressing the ill-conditioned problem of RANS equations. Shan et al.[11] employed a deep neural network to predict the eddy viscosity within the S-A turbulence model, reducing reliance on high-precision turbulence experimental data during model training using data assimilation technology.

Traditionally, research in data-driven turbulence modeling usually establishes the mapping relationship between the average flow variables and Reynolds stress or other turbulence quantities through techniques such as neural networks, random forests, etc. However, these mapping relationships tend to be unobservable and uninterpretable, presenting a significant challenge to the interpretability of machine learning applications in turbulence modeling. This lack of interpretability is a critical barrier that requires resolution for the effective application of machine learning in this turbulence modeling[12]. Recently, symbolic regression has gained attention as an innovative tool for data-driven turbulence modeling[13–16]. Symbolic regression aims to derive explicit equations that link input variables x_i with a target variable y. Unlike the "black box" models generated by other machine learning methods, the explicit nature of equations derived from symbolic regression allows for their physical meaning to be readily interpreted. Besides, this transparency facilitates the integration of physical prior knowledge, thereby enhancing both the interpretability and extrapolation capabilities of the models[10]. Moreover, incorporating the explicit equations derived from symbolic regression into CFD solvers can also help overcome the ill-conditioned problem often encountered in traditional data-driven turbulence modeling [6,10].

Despite the significant promise of symbolic regression in turbulence modeling, traditional algorithms in this domain, particularly those based on genetic programming (GP), encounter challenges related to extensive search spaces and slow learning speeds[17]. These limitations constrict the size of training datasets and the number of input features, consequently limiting the complexity of the symbolic expressions that can be generated. This, in turn, limits the predictive capabilities of the learned turbulence models. Research shows that within the search space of GP-based symbolic regression algorithms, most candidate expressions fail to adhere to the principle of unit consistency—that is, the units across equations or within addition and subtraction operations do not align[18]. Such inconsistencies render these expressions physically meaningless, leading to considerable inefficiencies in model learning. However, in turbulence modeling, it is a common practice to normalize flow quantities by the turbulence scale for modeling purposes. However, this normalization process results in the omission of unit information, which could otherwise be beneficial in data-driven turbulence modeling. The absence of these constraints leads to an expanded search space for algorithms, which adversely affects the learning efficiency and the interpretability of the models developed.

To address the limitations above, a unit-constrained turbulence modeling framework using symbolic regression is proposed. Within this framework, a new learned turbulence model for separated flow is developed. The performance and generalization capabilities of the learned turbulence model are then evaluated. The structure of this paper is as

follows: Section 2 outlines the turbulence closure problem, and introduces the proposed unit-constrained turbulence modeling framework using symbolic regression and the numerical methods used in this study. Section 3 details the case for training, input features, hyperparameters, and mesh. Section 4 applies the proposed turbulence modeling framework to the cases of flows over periodic hills. Section 5 presents the conclusions and outlook on future directions.

II. METHODOLOGY

In this section, we first introduce the turbulence closure issue and baseline turbulence model. Then, we introduce the proposed unit-constrained turbulence modeling framework using symbolic regression, detailing the algorithm structure and modeling process, and introduce the implementation method of unit constraint. Finally, the CFD solver and numerical methods used in the numerical simulations are described.

A. Turbulence closure

The Reynolds-averaged Navier-Stokes equation is the governing equation for RANS simulations. For incompressible flow, the equation is given by:

$$\frac{\partial \boldsymbol{U}}{\partial t} + \boldsymbol{U} \cdot \nabla \boldsymbol{U} = -\nabla p + \nu \nabla^2 \boldsymbol{U} + \nabla \cdot \boldsymbol{\tau} \tag{1}$$

where $\boldsymbol{U}$ is the time-averaged velocity vector, p is the time-averaged pressure, ν is the dynamic viscosity, and $\boldsymbol{\tau}$ is the Reynolds stress tensor. The Reynolds stress $\boldsymbol{\tau}$ is a 3×3 symmetric tensor. For two-dimensional flows, the Reynolds stress has four independent and non-zero components, which are τ_{11}、 τ_{22}、 τ_{33} and $\tau_{12}\left(=\tau_{21}\right)$; for three-dimensional flows, the Reynolds stress tensor has six independent and non-zero components, which are τ_{11}、 τ_{22}、 τ_{33}、 $\tau_{12}\left(=\tau_{21}\right)$、 $\tau_{13}\left(=\tau_{31}\right)$ and $\tau_{23}(=\tau_{32})$.

To close Eq. 1, LEVMs based on the Boussinesq assumption assume that the anisotropic Reynolds stress tensor $\boldsymbol{a}$ is linearly related to the mean strain rate tensor $\boldsymbol{S}$, given by:

$$\boldsymbol{a} = \boldsymbol{\tau} - \frac{2}{3}\rho k \delta_{ij} = -2\mu_t \boldsymbol{S} \tag{2}$$

where ρ represents density, k represents turbulent kinetic energy, δ_{ij} is the Kronecker delta, and μ_t is the eddy viscosity coefficient. The coefficient μ_t is determined by the scale of turbulence and is calculated differently across various turbulence models.

Widely used LEVMs include the S-A turbulence model[19], the *k*-*ε* model[20], the *k*-*ω* model[21], and the Shear Stress Transport (SST) model[22]. The standard *k*-*ε* model, proposed by B.E. Launder and D.B. Spalding, is one of the most commonly used turbulence models in engineering and serves as a benchmark in many data-driven turbulence modeling studies[2]. In the standard *k*-*ε* model, the eddy viscosity coefficient μ_t is calculated using the following equation[5]:

$$\mu_t = C_\mu \rho \frac{k^2}{\varepsilon} \tag{3}$$

where ε is the turbulent dissipation rate, C_μ is an empirical coefficient typically set to 0.09. The transport equations for turbulent kinetic energy k and turbulent dissipation rate ε are given by:

$$\frac{\partial k}{\partial t} + U_j \frac{\partial k}{\partial x_j} = \tau_{ij} \frac{\partial U_i}{\partial x_j} - \varepsilon + \frac{1}{\rho} \frac{\partial}{\partial x_j} \left[\left(\mu + \frac{\mu_t}{\sigma_k} \right) \frac{\partial k}{\partial x_j} \right] \tag{4}$$

$$\frac{\partial \varepsilon}{\partial t} + U_j \frac{\partial \varepsilon}{\partial x_j} = C_{\varepsilon_1} \frac{\varepsilon}{k} \tau_{ij} \frac{\partial U_i}{\partial x_j} - C_{\varepsilon_2} \frac{\varepsilon^2}{k} + \frac{1}{\rho} \frac{\partial}{\partial x_j} \left[\left(\mu + \frac{\mu_t}{\sigma_\varepsilon} \right) \frac{\partial \varepsilon}{\partial x_j} \right] \tag{5}$$

where μ is the dynamic viscosity, σ_k 、 C_{ε_1} 、 C_{ε_2} and σ_ε are model coefficients, typically set to:

$$\sigma_k = 1.0,\ C_{\varepsilon_1} = 1.44,\ C_{\varepsilon_2} = 1.92,\ \sigma_\varepsilon = 1.3 \tag{6}$$

In this study, the standard *k*-*ε* model is used as the baseline turbulence model to compute the baseline flow field and serves as the foundation for symbolic regression turbulence modeling.

B. Unit-constrained turbulence modelling framework using symbolic regression

1. Symbolic regression guided by unit constraint

Symbolic regression is traditionally implemented through GP techniques[23]. In recent years, deep learning has increasingly been applied to solve symbolic regression problems[18,24,25]. Tenachi et al.[18] introduced the Φ-SO symbolic regression algorithm guided by unit constraints based on recurrent neural networks (RNNs). This algorithm demonstrates notable efficiency and accuracy in expression learning. The turbulence modeling framework proposed in this study is based on the Φ-SO symbolic regression algorithm.

The Φ-SO algorithm operates based on RNNs and requires inputs to be in sequence form. Therefore, the first step is to transform the expression to be predicted into a symbolic sequence. This transformation is facilitated through the construction of a symbolic tree. Figure 1 demonstrates this process using the basic formula for hydrostatic pressure as an example. As shown in Fig. 1a, the right side of the equation consists of four independent variables: atmospheric static pressure p_a, fluid density ρ, gravitational acceleration g, height h, and two operators $\{+, \times\}$. Those quantities and operators are collectively referred to as the tokens constituting the expression. The collection of all possible tokens

that might contribute to the expression's formation is referred to as the tokens library. These tokens are organized into a tree structure based on their operational relationships, known as a symbolic tree, as shown in Fig. 1b. Each token within the symbolic tree is sequentially numbered from top to bottom and from left to right. By sequencing the tokens according to their assigned numbers, the corresponding symbolic sequence for the expression is derived, as illustrated in Fig. 1c. This process enables the representation of any expression as a corresponding symbolic sequence, thus rendering it compatible with processing by RNNs.

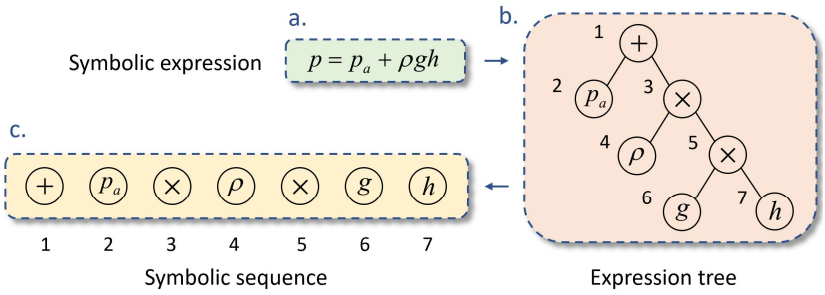

FIG. 1. The process of converting a symbolic expression into a symbolic sequence through an expression tree

The architecture of the Φ-SO algorithm is shown in Fig. 2. Within the algorithm, each RNN cell is aligned with a specific position in the symbolic sequence, with the total number of RNN cells matching the maximum allowed length for an expression. Each RNN cell receives an observation as input for its position, which includes the parent token and its unit, sibling token and its unit, previous token and its unit, the unit required at the current position, and the minimum number of operators needed to complete the expression. Taking the expression shown in Fig. 1 as an example, the third position in Fig. 1a corresponds to the third RNN cell (counting from left to right). It can be seen from Fig. 1b, the input (observation) for this RNN cell is the parent token "+", the sibling token "p_a", and the previous token "p_a", with their units being "\", "$M^1L^{-1}T^{-2}$", and "$M^1L^{-1}T^{-2}$" respectively, where M, L, and T represent mass, length, and time, respectively. In addition, the inputs also include the unit required at current position, i.e., "$M^1L^{-1}T^{-2}$", and the minimum number of tokens needed to complete the expression, which is "1" at current position. In the actual execution process of the algorithm, all tokens are assigned unique numbers as identifiers, and units are also represented in vector form; for instance, the unit of token "p_a" is described as {1, -1, -2}. After receiving its input, each RNN cell outputs a probability distribution for all potential tokens at the corresponding position through the softmax activation function. By applying a multiplier of 0 or 1 to each token, the algorithm can enforce any pre-established constraints, such as unit constraints, nesting constraints, etc.

To demonstrate the implementation of unit constraints, let's consider the prediction process for the fifth token in the expression shown in Fig. 1, assuming that the first four operators $\{+, p_a, \times, \rho\}$ in the expression are already accurately predicted. When unit constraints are applied to the expression, the algorithm initially determines the unit required at the current position. It is found that the required unit is "$M^0L^2T^{-2}$", indicating that tokens such as "p_a", "ρ", "g", and "h" from the token library are not possible candidates for this position due to unit mismatch. Consequently, a mask vector is generated for all tokens, wherein positions corresponding to ineligible tokens are assigned a value of 0, while the rest are set to 1. This mask vector is then multiplied by the probability distribution vector produced by the RNN cell, effectively reducing the probabilities of the ineligible tokens to 0. This mechanism allows for the integration of any predefined constraints, such as unit constraints, into the prediction process, ensuring that the generated expression adheres to these constraints.

Upon the application of prior constraints, the algorithm selects the tokens with the highest probability as the sampling tokens. Eventually, these sampled tokens are positioned to formulate the symbolic expression as output, following the reverse process in Fig. 1 (c→b→a).

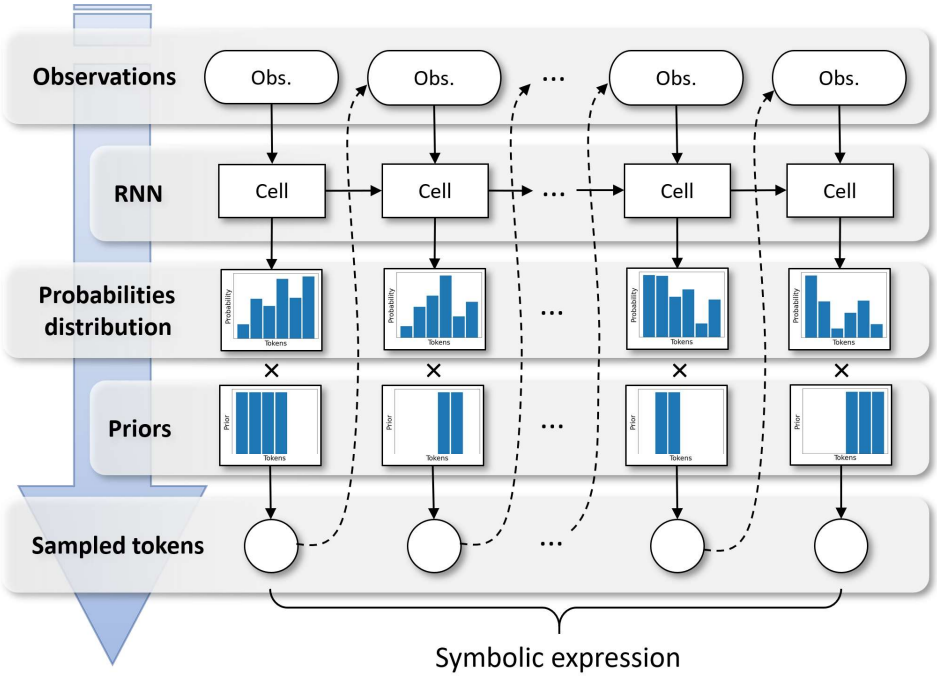

FIG. 2. Diagram of the Φ-SO Symbolic regression algorithm architecture

To learn knowledge from data, the RNN needs to be trained via the backward propagation process. Typically, Neural networks are trained using the gradient descent (GD) method. However, in the context of symbolic regression

problems, the non-differentiability of the cost function prevents the direct application of the GD method for training network. Therefore, the Φ-SO algorithm employs a reinforcement learning strategy to train the network and uses a risk-seeking policy to optimize the performance of symbolic regression. The risk-seeking policy calculates the loss value based on a subset of candidate expressions with the highest fitness (i.e., reward values) in a batch, meaning it only learns from the "best-performing" subset of expressions. This approach aligns with the objective of symbolic regression, which seeks to find the best expression that most closely approximates the target, rather than maximizing the average predictive accuracy of all expressions. The effectiveness of the risk-seeking strategy in symbolic regression tasks has been well-documented [25]. For detailed information about the Φ-SO symbolic regression algorithm and the risk-seeking strategy, please refer to the original papers by Tenachi et al.[18] and Petersen et al.[25]

2. Unit-constrained symbolic regression turbulence modeling

Based on the Φ-SO symbolic regression algorithm, a unit-constrained turbulence modeling framework using symbolic regression is established, as illustrated in Fig. 3. The proposed framework comprises the following four steps:

a. Acquisition of baseline flow field and high-precision turbulence data

Conducting RANS simulation with a baseline LEVM model to acquire the baseline flow field. Subsequently, obtaining high-precision turbulence data through experiments, DNS, or LES simulations, or by accessing existing open-source high-precision turbulence datasets.

b. Calculation of mean flow features and Reynolds stress deviation

Using the mesh cell centers from the RANS simulation as sampling points to extract mean flow features, denoted as q_i at each point, where i=1, 2, 3, …, n, and n is the number of pre-selected mean flow features. The Reynolds stress tensor $\boldsymbol{\tau}_{\mathrm{RANS}}$ at each sampling point is extracted from the baseline flow field. This tensor is then compared with the high-precision Reynolds stress data $\boldsymbol{\tau}_{\mathrm{hp}}$ obtained from a high-accuracy turbulence dataset, to calculate the Reynolds stress deviation tensor $\Delta\boldsymbol{\tau} = \boldsymbol{\tau}_{\mathrm{hp}} - \boldsymbol{\tau}_{\mathrm{RANS}}$ at each sampling point.

c. Derivation of Reynolds stress deviation expression via symbolic regression

Using the mean flow features, q_i, obtained in the preceding step as input variables, and the Reynolds stress deviation tensor, $\Delta\boldsymbol{\tau}$, as the target variable. Using the unit-constrained symbolic regression algorithm introduced earlier to derive explicit equations linking each component of the Reynolds stress deviation to the mean flow features. As elucidated in Section 2.1, for two-dimensional turbulence, the deviation tensor has four independent, non-zero

components, requiring the establishment of four scalar algebraic equations. For three-dimensional turbulence, the deviation tensor has six independent, non-zero components, requiring the establishment of six scalar algebraic equations.

Upon deriving the equations for Reynolds stress deviation $\Delta\boldsymbol{\tau}(q_i)$, these equations are integrated as correction terms into the constitutive equations of the original baseline turbulence model, as depicted in Eq. 7. This integration results in the formulation of a new, learned turbulence model. The methodologies for calculating turbulent viscosity μ_t, turbulent kinetic energy k, and other turbulence quantities remain aligned with those of the baseline turbulence model.

$$\boldsymbol{\tau} = \frac{2}{3}\rho k\delta_{ij} - 2\mu_t \boldsymbol{S} + \boldsymbol{\Delta\tau}(q_i) \tag{7}$$

d. Numerical simulation using the learned turbulence model

A loose coupling method is adopted to couple the learned turbulence model with the RANS solver. This method only calculates the Reynolds stress deviation during the initial step of the numerical simulation, with its values remaining constant throughout the subsequent iteration process until convergence is achieved. Finally, using the baseline flow field obtained in the first step as the initial flow field, the learned turbulence model is applied in numerical simulation to obtain an improved turbulence field.

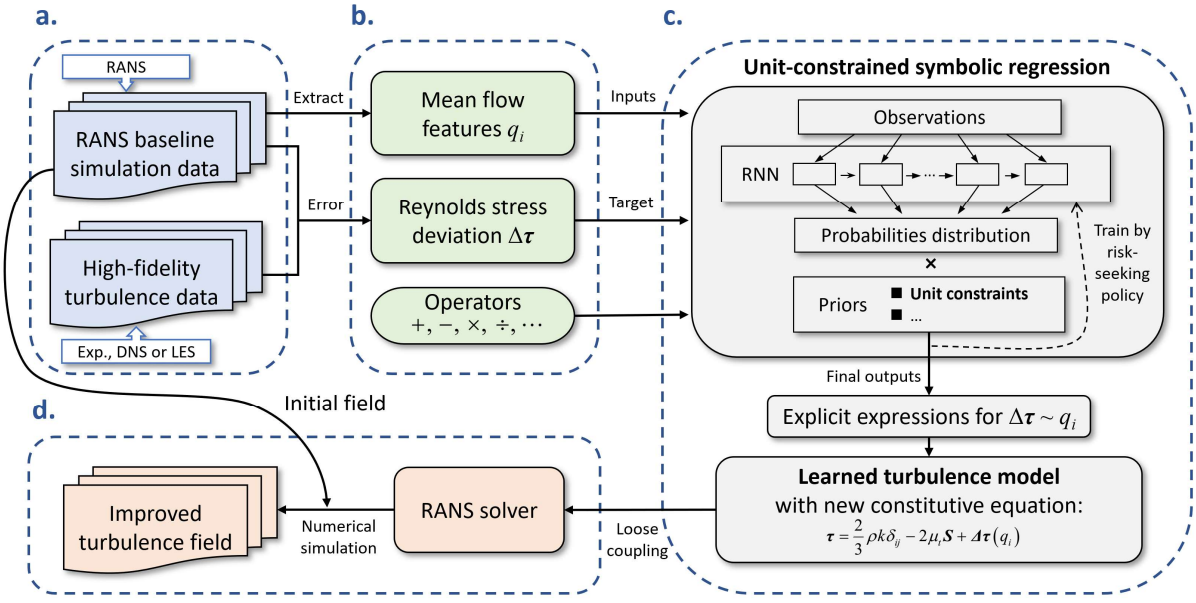

FIG. 3. A sketch map of the symbolic regression turbulence modeling framework with unit constraint

C. Numerical method

Numerical simulations in this study are conducted using the open-source software OpenFOAM. The incompressible solver simpleFoam is used to perform steady-state simulations. The convective terms within the governing equation are solved using a second-order upwind scheme, whereas the remaining terms are solved using a second-order central difference scheme. The standard k-ε model proposed by B.E. Launder and D.B. Spalding is selected as the baseline turbulence model. A detailed introduction to the model is provided in Section 2.1 and Reference 20.

III. CASE SETUP

Section 2 introduced the proposed unit-constrained turbulence modeling framework using symbolic regression. To evaluate the efficacy of the proposed framework in large separated turbulence, the subsequent sections of this paper employ the flow over periodic hills as a case study to validate the modeling capabilities of the proposed framework. This section introduces the basic characteristics of the flow over periodic hills, the selection for input features, the hyperparameters, and the mesh configuration.

A. Flow over periodic hills

The flow over two-dimensional periodic hills is a commonly used validation case in studying separated turbulence modeling. Xiao et al.[26] presented a series of periodic hills cases with parameterized geometries and provided corresponding DNS datasets. These datasets have been widely used in data-driven turbulence modeling research for separated flows[2,10,14,15].

Figure 4 provides a schematic diagram of the periodic hills with parameterized geometries. The left and right boundaries are subject to periodic boundary conditions, and the top and bottom boundaries are no-slip wall boundaries. The flow enters from the left inlet along the x-direction. Upon encountering the first hill on the leeward side, an adverse pressure gradient prompts flow separation, leading to the formation of a recirculation zone. The separated flow reattaches downstream, flows over the windward side of the right second hill, and finally exits through the right boundary. For the periodic hills with parameterized geometries, the total height L_y normalized by the hill height H, L_y/H, is fixed at 3.036. The total length of the domain along the x-direction, L_x, is controlled by the parameter α. As α increases, L_x will also increase, which in turn stretches the bottom wall along x-axis and reduces the slope of the hill.

The height of hills H and the total height of the domain L_y do not change with variations in α. The equations defining the shape of the hill and the variation of L_x with parameter α are detailed in Appendix A.

In this study, the flows over periodic hills for α=0.8, 1.0, and 1.2 are used as training and testing cases for modeling.

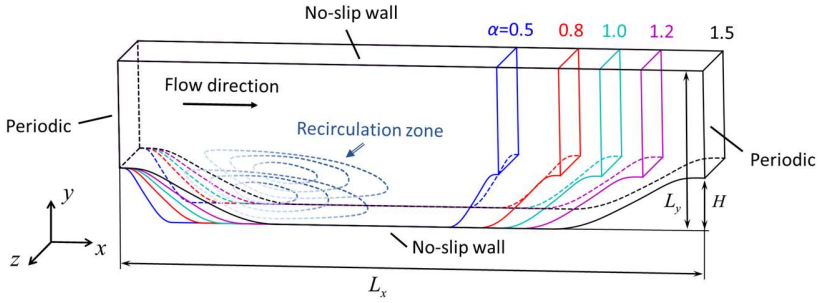

FIG. 4. A sketch of the flow over periodic hills with parameterized geometries

B. Mean flow features as input variables

The objective of symbolic regression turbulence modeling is to establish explicit equations linking mean flow features q_i to Reynolds stress deviations $\Delta\boldsymbol{\tau}$. Therefore, the selection of mean flow features will directly influence the efficacy of modeling. Considering equation solvability, computational efficiency, and physical significance, the selection of mean flow features should follow these principles:

(1) The features must pertain solely to the mean flow or be derivable from existing turbulence transport equations, ensuring the resultant equations are closed and do not impose additional computational demands.

(2) The features should be able to reflect the characteristics of turbulent flow and have clear physical meanings, ensuring that the results of symbolic regression are interpretable.

(3) The features should satisfy Galilean invariance.

Based on the principles above, this study selects eight mean flow features that satisfy Galilean invariance proposed by Wang et al. [2] as input features, denoted respectively by $q_1, q_2, \cdots, q_8$. The expressions and physical meanings of these eight features are shown in Table I. Among them, q_1 represents the Q criterion, a parameter commonly used in CFD for identifying flow structures; q_2 represents turbulent kinetic energy, indicating the isotropic part of the Reynolds stress tensor, which can be derived from the existing k-equation (see Eq. 4); q_3 represents the turbulence Reynolds number based on wall distance, which is an important parameter for distinguishing between boundary layers and shear flows; q_4 represents the pressure gradient along the streamline; q_5 represents the time scale of turbulence, which can be calculated from the existing k-equation (see Eq. 4) and ε-equation (see Eq. 5); q_6 represents the normal stress part

of pressure; q_7 represents a measure of the deviation in orthogonality between velocity and its gradient, characterizing the deviation between the flow and parallel shear flows; q_8 represents the convection of turbulent kinetic energy.

TABLE I. Mean flow features as symbolic regression input

		Physical meanings
q_1	$\frac{1}{2}\left(\|\boldsymbol{R}\|^2-\|\boldsymbol{S}\|^2\right)$	Q criterion
q_2	k	Turbulent kinetic energy
q_3	$\min\left(\frac{\sqrt{k}d}{50\nu},2\right)$	Turbulent Reynolds number based on wall distance
q_4	$U_k\frac{p}{x_k}$	Pressure gradient along the streamline
q_5	$\frac{k}{\varepsilon}$	Turbulence time scale
q_6	$\sqrt{\frac{\partial p}{\partial x_i}\frac{\partial p}{\partial x_i}}$	Pressure normal stress
q_7	$\left\|U_iU_j\frac{\partial U_i}{\partial x_j}\right\|$	Non-orthogonality between velocity and its gradient
q_8	$U_i\frac{\partial k}{\partial x_i}$	Turbulent kinetic energy convection

In addition to the eight flow above features, the token library used in this paper also includes five scalar operator tokens and one non-dimensional free constant: {+, -, ×, ÷, $(\cdot)^2$, C}, where $(\cdot)^2$ denotes the square operator, and C represents the free constant, a total of 14 operators. It is worth mentioning that in existing data-driven turbulence modeling research, Reynolds stresses and input features are often made non-dimensional to avoid non-physical issues arising from unit inconsistencies. In this study, since unit information is an essential constraint for symbolic regression, the features above are not been nondimensionalized.

C. Learning parameters

This study employs a risk-seeking strategy to facilitate the learning of the RNN network. The ADAM optimizer is utilized to update network parameters. The optimization of the free constant term in the learned expression is carried out through an embedded inner loop using the LBFGS method, with 15 iterations in the inner loop. In the risk-seeking gradient policy, the fitness of an expression is measured by the closeness of the calculated result of the learned expression to the target value. The fitness of an expression is quantified using a reward value, where a higher value indicates a smaller error between the symbolic regression result and the true value. The calculation of the reward value is given by:

$$R = \frac{1}{1 + \mathrm{NRMSE}} \tag{8}$$

where NRMSE stands for Normalized Root Mean Square Error, and its calculation method is as follows:

$$\mathrm{NRMSE} = \frac{1}{\sigma_{\Delta\tau}} \sqrt{\frac{1}{N} \sum_{j=1}^{N} \left(\Delta\tau - f(q_i)\right)^2} \tag{9}$$

where $\sigma_{\Delta\tau}$ is the standard deviation of the target values $\Delta\tau$, N is the size of the dataset, and $f(q_i)$ is the result calculated by learned expression.

The configuration of hyperparameters plays a crucial role in efficiently executing symbolic regression tasks. In this study, each RNN cell consists of 1 hidden layer with 128 neurons; the neural network is trained for 60 epochs, with a batch size of 1000; the risk factor, representing the proportion of preferred expressions selected in the risk-seeking policy among all expressions, is set to 5% in this study; the learning rate is set to 0.0001. To reduce the time cost of model training and CFD computations, the maximum length of predicted expressions is set to 15, meaning that expressions can consist of up to 15 tokens. A detailed overview of the hyperparameter settings is provided in Table II. All the hyperparameters underwent meticulous tuning before training to achieve the optimal balance between model prediction accuracy and training cost.

TABLE II. Hyper-parameters

Hyper-parameter	Value
RNN architecture	128×1
Num. of epoch	60
Risk factor	5%
Batch size	1000
Entropy weight	0.005
Gamma decay	0.7
Max length	15
Learning rate	0.0001

D. Mesh and mesh independence study

In the numerical simulation part of this paper, a structured mesh, as shown in Fig. 5, is used to discretize the computational domain. The mesh is appropriately refined near the walls and corners to capture the boundary and recirculation region accurately. To verify the mesh independence of the numerical results, three sets of meshes, namely Mesh A, Mesh B, and Mesh C, from sparse to dense, are generated for mesh independence validation. Table III provides the distribution of mesh points along the streamwise (*x*-axis), wall-normal (*y*-axis), and spanwise (*z*-axis) as

well as the non-dimensional first-layer mesh height $\Delta y/H$ for the three mesh sets. Since this study focuses on two-dimensional turbulent flow, the number of mesh points in the spanwise (z-axis) for all three mesh sets are set to 2.

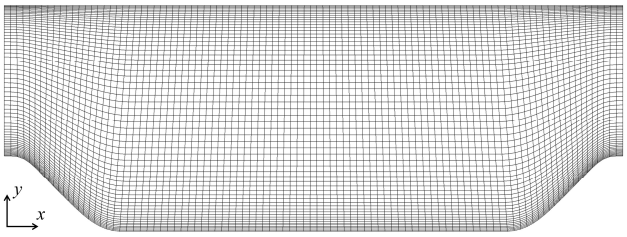

FIG. 5. Mesh of computation domain

TABLE III Summary of mesh resolution along different directions

Mesh	Streamwise (x-direction)	Wall-normal (y-direction)	Spanwise (z-direction)	Δy/H
Mesh A	100	60	2	9×10^{-3}
Mesh B	140	80	2	6×10^{-3}
Mesh C	160	100	2	3×10^{-3}

Figure 6 presents the streamwise velocity (normalized by the bulk velocity U_b at the hill crest, where $U_b = 0.028$m/s) profiles for flow over periodic hills at x/H=1.5 for each mesh, as obtained by the standard k-ε model under the conditions of α=0.8 and Re=5600. It can be observed that the streamwise velocity distributions obtained from these three meshes are approximately the same. Upon closer examination of the curves, a relatively significant discrepancy is observed between the velocity distributions obtained from Mesh A and Mesh B, while the results from Mesh B and Mesh C exhibit good agreement. Therefore, Mesh B and Mesh C meet the requirements of mesh independence. Considering both computational efficiency and accuracy, Mesh B is selected to compute the baseline flow field and subsequent validation of the learned models.

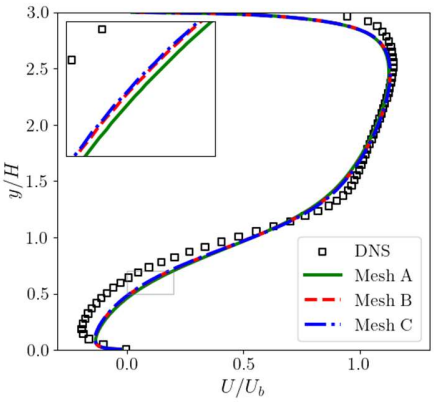

FIG. 6. Normalized streamwise velocity profile at x/H=1.5 calculated by three different meshes (α=0.8, Re=5600)

IV. RESULTS

To verify the effectiveness of the proposed framework in large separated flow, this section first uses the standard k-ε model to perform numerical simulation of the flow over periodic hills and obtain the baseline flow field. Then, the eight mean flow features given in Section 3 and the Reynolds stresses are derived. By comparing to the Reynolds stresses extracted from the high-fidelity DNS turbulence dataset, the Reynolds stress deviations are calculated. The Reynolds stress deviations and the mean flow features are used as inputs for the symbolic regression learning to obtain explicit equations for the Reynolds stress deviation. These equations are then embedded as a correction term into the constitutive equation of the original turbulence model to establish a learned turbulence model. To validate the learned turbulence model's capability in simulating and generalizing in large separated turbulence flows, numerical simulations of periodic hills with the same geometry as the training case and different geometries are conducted.

A. Learning result

In this study, the flow over periodic hills under the condition of α=0.8 was used as the training case. The flow Reynolds number, based on the wall height H and the bulk velocity U_b at the hill crest was 5600. The numerical methods and mesh described in Section 3 were employed, and the standard k-ε model was used to compute the baseline flow field. The computation was performed for 20,000 iterations, ensuring convergence by examining the residuals.

The Reynolds stresses obtained from the baseline flow field, along with the flow characteristic quantities and DNS Reynolds stress data, were used as inputs for the symbolic regression algorithm. After training for 60 epochs, explicit equations for the four independent, non-zero components of the Reynolds stress tensor discrepancies were obtained. The hyperparameter configuration used for the training is detailed in Table 2. The training was conducted on a high-performance computer with an Intel Core i5-10600KF processor and 64GB of RAM, utilizing a single-core CPU. Each of the four Reynolds stress discrepancy components was trained for 60 epochs, with the total training time amounting to approximately 50 minutes.

The variation of the reward value of the best expression in a batch with the number of epochs during the learning is shown in Fig. 7. As shown in the figure, the reward values corresponding to the four Reynolds stress discrepancy components initially increase rapidly with the number of epochs and then stabilize, indicating that the symbolic regression training has converged within the selected number of epochs.

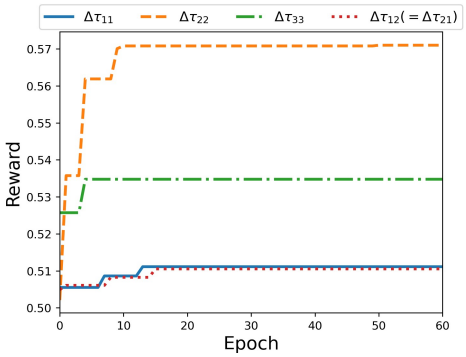

FIG. 7. The variation of reward values with the epochs during the learning process

The explicit equations for the four components of the Reynolds stress discrepancy tensor obtained through symbolic regression are as follows:

$$\begin{cases} \Delta\tau_{11} = \dfrac{q_2 q_3^2}{(1+2q_3)^2} \\ \Delta\tau_{22} = -\dfrac{q_2}{2+q_3} \\ \Delta\tau_{33} = q_2 q_3^2 (q_3 - 2)^2 \\ \Delta\tau_{12}\left(=\Delta\tau_{21}\right) = \dfrac{q_5 q_8}{3q_3 + 1} \end{cases} \tag{10}$$

Eq. 10 shows that the trained Reynolds stress discrepancies are solely related to four mean flow features: turbulent kinetic energy q_2, turbulent Reynolds number q_3 turbulent time scale q_5, and turbulent kinetic energy convection q_8. Specifically, the three normal stress components of the Reynolds stress discrepancy, $\Delta\tau_{11}$, $\Delta\tau_{22}$, and $\Delta\tau_{33}$, are only functions of q_2 and q_3, while the shear stress component $\Delta\tau_{12}$ is determined by q_3, q_5, and q_8. By examining the units on both sides of the equations and the addition or subtraction, it is confirmed that the obtained expressions adhere to the principle of unit consistency.

By reconstructing the Reynolds stress deviation components given by Eq. 10 into the Reynolds stress tensor, and incorporating it as a correction term into the constitutive equation of the original turbulence model, the modified constitutive equation shown in Eq. 7 is obtained, thereby establishing a new learned turbulence model.

B. Performance in the training geometry

To validate the predictive accuracy of the learned model for separated turbulence flow, numerical simulations were performed using the learned model on the periodic hills flow (α=0.8) with the same geometry as the training case. The results were compared with those obtained from the baseline standard k-ε model and DNS results.

Figure 8 presents the distributions of the non-dimensional anisotropic Reynolds stress tensor components $\boldsymbol{a}/(U_b)^2$ for the flow over periodic hills (α=0.8, training case) obtained from the standard k-ε model and the learned turbulence model, along with comparisons to DNS results. Comparing the first row (standard k-ε model results) and the third row (DNS results), it is evident that the spatial distributions of the anisotropic Reynolds stress components from the standard k-ε model significantly differ from the DNS results, with varying discrepancies across different components. For component a_{11}, the standard k-ε model underestimates its values in the non-parallel free shear flow region (y/H=0.8~1.5) and near the crest of the windward side of the hill (x/H≈8.0). For a_{22}, the standard k-ε model overestimates its values in the non-parallel free shear flow region and near the crest of the windward side of the hill. For a_{33}, the standard k-ε model's results are nearly zero across the entire domain, failing to capture its spatial distribution. For the shear stress component a_{12}, the predictions from the standard k-ε model are generally close to the DNS results, but the values are significantly underestimated near the windward side of the hill.

Comparing the second row (learned model results) and the third row (DNS results), it can be seen that the learned model significantly improves the prediction accuracy of the anisotropic Reynolds stress components compared to the standard k-ε model. For the normal stress component a_{11}, the learned model correctly captures the sign and distribution trend of a_{11} in the non-parallel free shear flow region. For component a_{22}, near the crest of the windward side of the hill, the learned model reduces the overestimation compared to the standard k-ε model, bringing the values closer to the DNS results. Additionally, the learned model correctly captures the sign and distribution trend of a_{22} in the non-parallel free shear flow region. For component a_{33}, the learned model captures its distribution near the bottom wall but fails to predict the distribution further away from the wall accurately, and overestimates the values near the upper wall. Nevertheless, similar to the standard k-ε model, the learned model correctly predicts the sign of a_{33} in the non-parallel free shear flow region. For component a_{12}, the learned model shows improvements over the standard k-ε model, particularly near the windward side of the hill.

Figure 9 shows the error distributions of the anisotropic Reynolds stress tensor components for the flow over periodic hills (α=0.8, training case) obtained from the standard k-ε model and the learned turbulence model. The figure indicates that the errors in the anisotropic Reynolds stress tensor components obtained from the learned model are significantly smaller than those from the standard k-ε model, with the most notable improvements observed in the predictions of a_{11}, a_{22}, and a_{12}. The primary areas where the anisotropic Reynolds stress error is reduced are concentrated in the non-parallel free shear flow areas and near the windward side of the hill. The non-parallel free

shear flow area is precisely the typical region where RANS simulations often experience prediction inaccuracies in such flows[27]. It is evident that the learned model established in this paper significantly improves the prediction accuracy of the original standard k-ε model for anisotropic Reynolds stress.

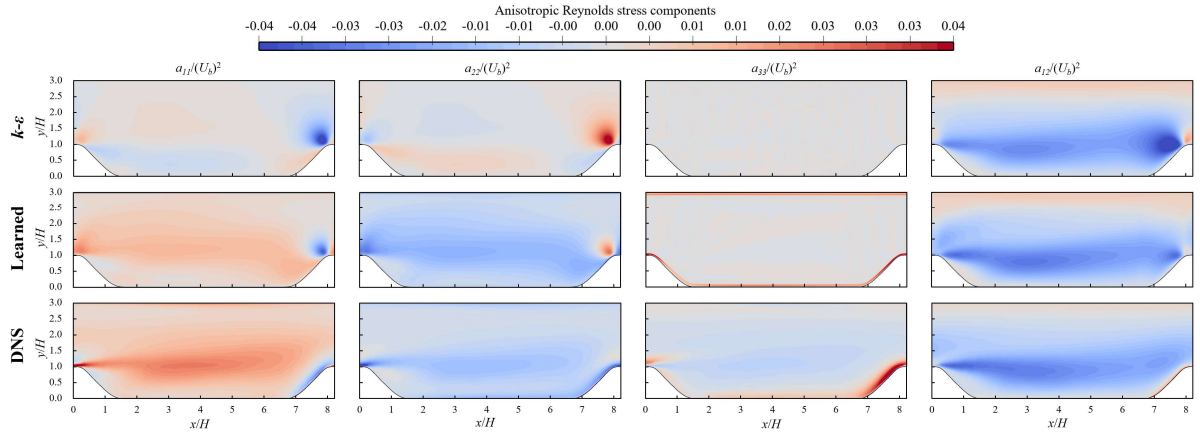

FIG. 8. The non-dimensional anisotropic Reynolds stress components obtained by the standard k-ε model and the learned model, compared with DNS data. (α=0.8, training case)

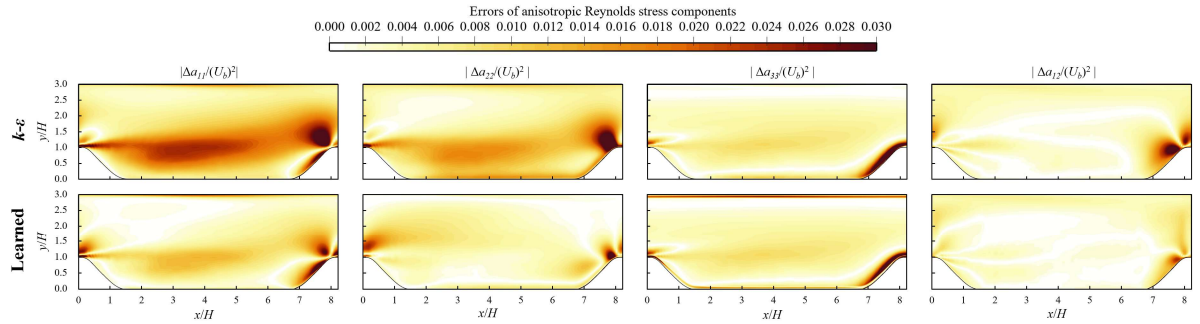

FIG. 9. The errors of non-dimensional anisotropic Reynolds stress components obtained by the standard k-ε model and the learned model. (α=0.8, training case)

From the analysis above, it can be seen that the learned model shows significant improvements in the accuracy of Reynolds stress predictions. However, quantities such as flow velocity are often of greater interest in practical engineering applications. Additionally, Wu et al. [6] pointed out that in data-driven turbulence modeling studies, even if the Reynolds stresses have high accuracy (errors less than 0.5%), the resulting velocity field can still exhibit significant errors (up to 35%). Therefore, further analysis of the learned model's performance in predicting the velocity field is necessary.

Figure 10 presents the non-dimensional streamwise velocity distributions and streamlines for the flow over periodic hills (α=0.8, training case) obtained from the standard k-ε model and the learned turbulence model, compared

with DNS results. As shown in Fig. 10, it can be seen that the standard k-ε model, the learned turbulence model, and the DNS all capture the flow separation on the leeward side of the hill (x/H=0~4), but there are differences in the shape and size of the recirculation zones obtained by the three methods. Compared to the DNS results, the standard k-ε model predicts a further downstream separation point and a reattachment point that is further upstream, resulting in a significantly smaller recirculation zone than that observed in the DNS results. In contrast, the learned model yields separation and reattachment points, as well as the size of the recirculation zone, that are much closer to the DNS results, indicating that the learned model has a higher accuracy in capturing flow separation.

Figure 11 shows the non-dimensional streamwise velocity profiles at different streamwise positions (x/H=0.5 to 7.5, with a step size of 1.0) for the flow over periodic hills (α=0.8, training case) obtained from the standard k-ε model and the learned turbulence model, compared with DNS results. As shown in Fig. 11, it can be seen that both the standard k-ε model and the learned turbulence model capture the general trend of the streamwise velocity profiles at different streamwise positions. However, in the recirculation zone (x/H=0~4), the streamwise velocity distributions obtained from the standard k-ε model show significant discrepancies compared to the DNS results. Specifically, the standard k-ε model underestimates the velocity in the recirculation zone and fails to capture the near-wall recirculation at x/H=3.5. In contrast, the learned model not only accurately captures the streamwise velocity distribution within the recirculation zone but also shows higher accuracy in predicting the velocity distribution above the recirculation zone (x/H=0~4.0, y/H=1.0~2.0). Additionally, as shown in Fig. 8, although the learned model overestimates the anisotropic Reynolds stress component a_{33} near the upper wall, this overestimation does not manifest in the corresponding region of the velocity field.

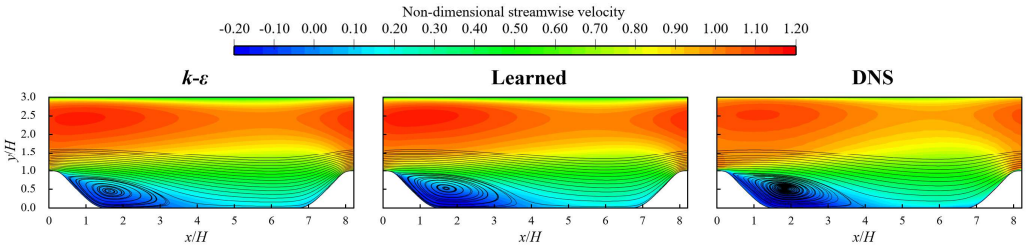

FIG. 10. The non-dimensional streamwise velocity distribution and streamlines obtained by the standard k-ε model and the learned model, compared with DNS data. (α=0.8, training case)

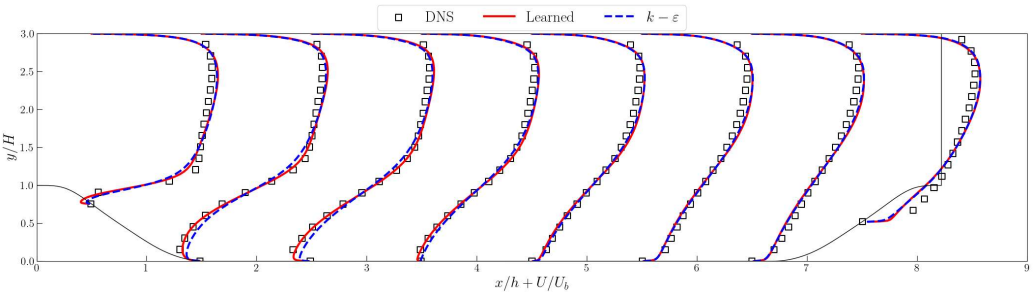

FIG. 11. The non-dimensional streamwise velocity profile obtained by the standard k-ε model and the learned model, compared with DNS data. (α=0.8, training case)

From the results above, it can be seen that the learned model derived from unit-constrained symbolic regression turbulence modeling not only achieves higher accuracy in predicting the anisotropic Reynolds stress tensor compared to the original k-ε model but also demonstrates improved accuracy in predicting the extent of separation and the streamwise velocity profiles.

C. Beyond the training geometry

In data-driven turbulence modeling research, a common issue is the insufficient generalization performance of the established models. This means that when the freestream conditions or the geometry of the flow field change, the model's performance can deteriorate significantly compared to its performance under the training conditions, thereby limiting its applicability. To validate the generalization performance of the learned model, numerical simulations were conducted using the learned turbulence model on flows over periodic hills with different geometries (α=1.0 and α=1.2) compared to the training case (α=0.8). The flow Reynolds number, based on the wall height H and the bulk velocity U_b at the hill crest was 5600. The initial flow field for the numerical simulations was obtained through the standard k-ε model. The numerical methods and mesh remained consistent with those described in Section 3.

Figures 12 and 13 show the distributions of the non-dimensional anisotropic Reynolds stress tensor components and their absolute errors for the flow over the periodic hill (α=1.0, non-training case) obtained from the standard k-ε model and the learned model respectively. As shown in Fig. 12, it can be observed that similar to the training case (α=0.8), the prediction errors of the anisotropic Reynolds stress tensor from the standard k-ε model are primarily located in the non-parallel free shear flow region (y/H=0.8~1.5) and near the windward side of the hill ($x/H\approx$8.5). However, due to the increased α, which results in a more gradual slope of the hill, the adverse pressure gradient is reduced, and the flow separation is weakened. Consequently, the prediction errors of the anisotropic Reynolds stresses

from the standard k-ε model are relatively smaller than the training case (α=0.8). Compared to the standard k-ε model, the learned model still shows significant improvements in the accuracy of the anisotropic Reynolds stress tensor prediction, with the most notable enhancements in the predictions of the components a_{11}, a_{22}, and a_{12}.

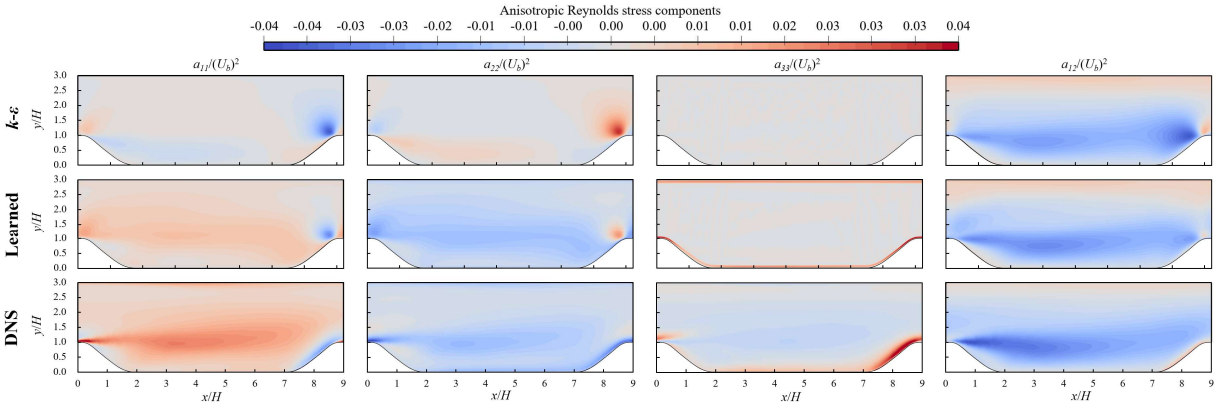

FIG. 12. The non-dimensional anisotropic Reynolds stress components obtained by the standard k-ε model and the learned model, compared with DNS data. (α=1.0, non-training case)

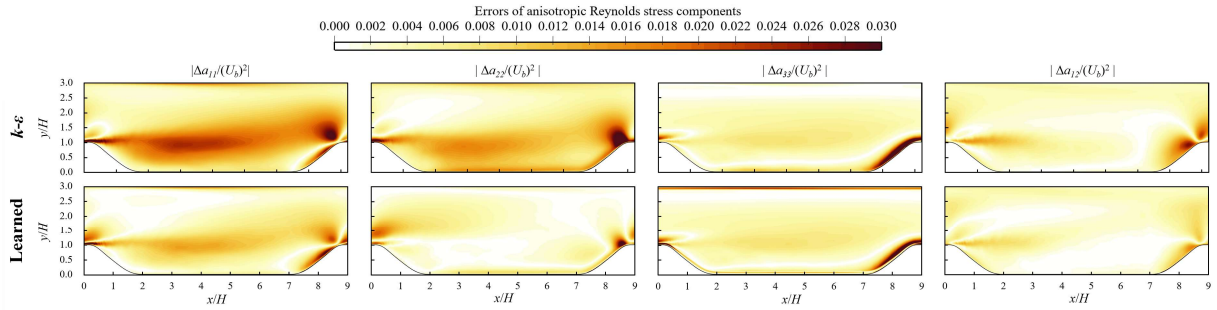

FIG. 13. The errors of non-dimensional anisotropic Reynolds stress components obtained by the standard k-ε model and the learned model. (α=1.0, non-training case)

Figure 14 shows the non-dimensional streamwise velocity distributions and streamlines for the flow over the periodic hill (α=1.0, non-training case) obtained from the standard k-ε model and the learned turbulence model, compared with DNS results. Figure 15 presents the non-dimensional streamwise velocity profiles at different streamwise positions for the same case. As shown in Fig. 14, it can be observed that due to the increased α, resulting in a more gradual slope of the hill, the size of the recirculation zone is slightly reduced compared to the α=0.8 case, as shown by the standard k-ε model, the learned turbulence model, and the DNS results. Compared with the DNS results, the standard k-ε model significantly underestimates the size of the recirculation zone, and the degree of underestimation is more significant than that in the training case (α=0.8). In contrast, the learned model provides a more reasonable prediction of the recirculation zone size, although the reattachment point predicted by the learned

model is still slightly upstream compared to the DNS results. As shown in Fig. 15, it can be seen that the learned model's streamwise velocity profiles at different streamwise positions are closer to the DNS results compared to the standard k-ε model. Although the learned model's accuracy in predicting the velocity distribution is not as high as in the training case, it still significantly outperforms the standard k-ε model.

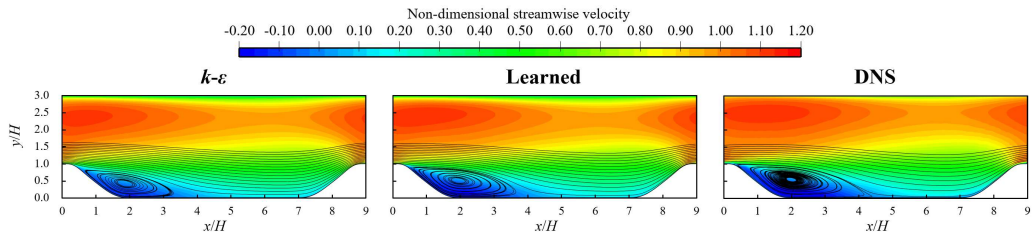

FIG. 14. The non-dimensional streamwise velocity distribution and streamlines obtained by the standard k-ε model and the learned model, compared with DNS data. (α=1.0, non-training case)

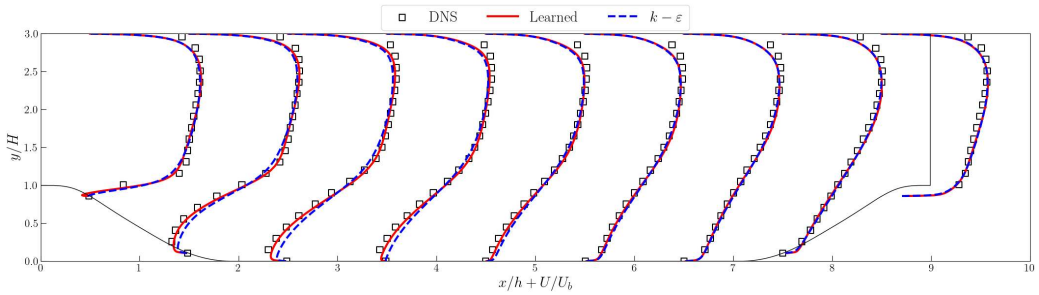

FIG. 15. The non-dimensional streamwise velocity profile obtained by the standard k-ε model and the learned model, compared with DNS data. (α=1.0, non-training case)

To further validate the generalization capability of the learned model, numerical simulations were conducted for the flow over periodic hills with α=1.2, which has a geometry more different from the training case. Figures 16 and 17 present the distributions of the non-dimensional anisotropic Reynolds stress tensor components and their absolute errors for the flow over periodic hills (α=1.2, non-training case) obtained from the standard k-ε model and the learned turbulence model, respectively. As shown in Figs. 16 and 17, it can be observed that under the condition of α=1.2, the distributions of the anisotropic Reynolds stresses and their errors obtained from the standard k-ε model are generally reduced compared to the conditions of α=0.8 and 1.0. However, in the non-parallel shear flow region, the errors in the anisotropic Reynolds stresses are slightly larger compared to other conditions. As shown in Fig. 17, it is evident that even for the α=1.2 case, which has a geometry significantly different from the training case, the learned model still demonstrates significantly higher accuracy in predicting the anisotropic Reynolds stresses compared to the original k-ε model.

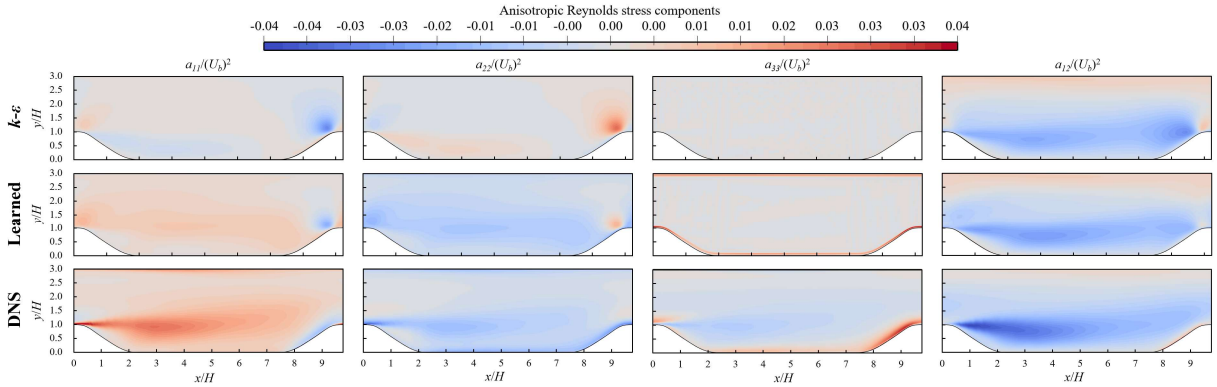

FIG. 16. The non-dimensional anisotropic Reynolds stress components obtained by the standard k-ε model and the learned model, compared with DNS data. (α=1.2, testing case)

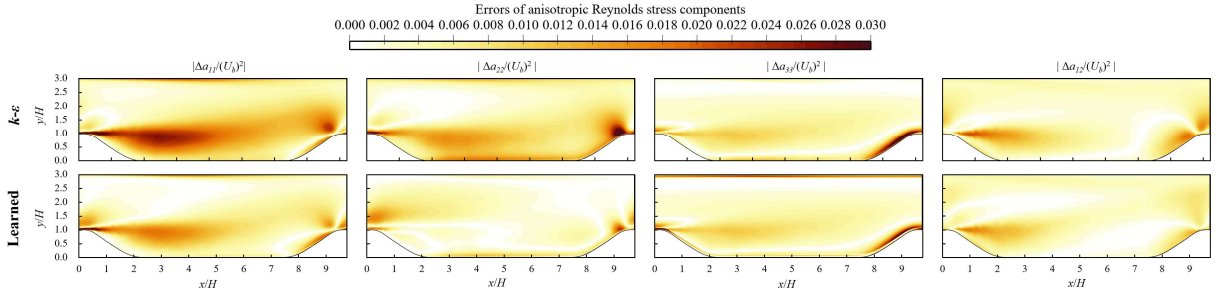

FIG. 17. The errors of non-dimensional anisotropic Reynolds stress components obtained by the standard k-ε model and the learned model. (α=1.2, non-training case)

Figure 18 shows the non-dimensional streamwise velocity distributions and streamlines for the periodic hill flow (α=1.2, non-training case) obtained from the standard k-ε model and the learned model, compared with DNS results. Figure 19 presents the non-dimensional streamwise velocity profiles at different streamwise positions for the same case. As shown in Fig. 18, it can be observed that due to the further flattening of the hill slope with α=1.2, the size of the recirculation zone is further reduced compared to the conditions of α=0.8 and 1.0. Despite this, the standard k-ε model still significantly underestimates the size of the recirculation zone. The standard k-ε model results show that the flow separation point is located around x/H=1.0, which is noticeably later than the DNS result ($x/H\approx$0.5). In contrast, the learned model provides a more accurate prediction of the recirculation zone size, with the flow separation point approximately located at $x/H\approx$0.6, which is closer to the DNS result. As shown in Fig. 19, compared with the standard k-ε model, the prediction model is more accurate in predicting the streamwise velocity profiles, especially in the recirculation zone within the range of x/H=0~4. The learned model's prediction accuracy in this region is even higher than that for the α=1.0 case, which is geometrically closer to the training case.

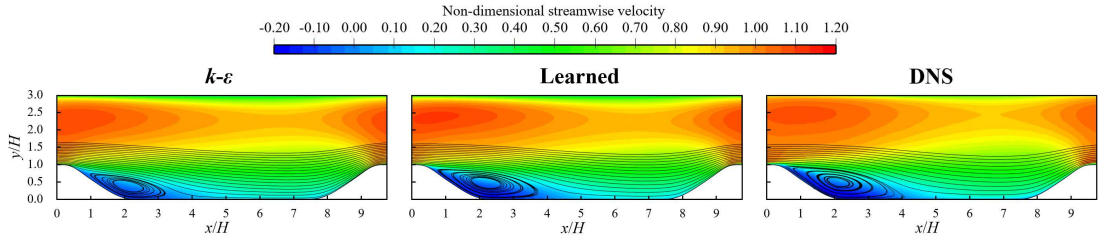

FIG. 18. The non-dimensional streamwise velocity distribution and streamlines obtained by the standard *k-ε* model and the learned model, compared with DNS data. (α=1.2, non-training case)

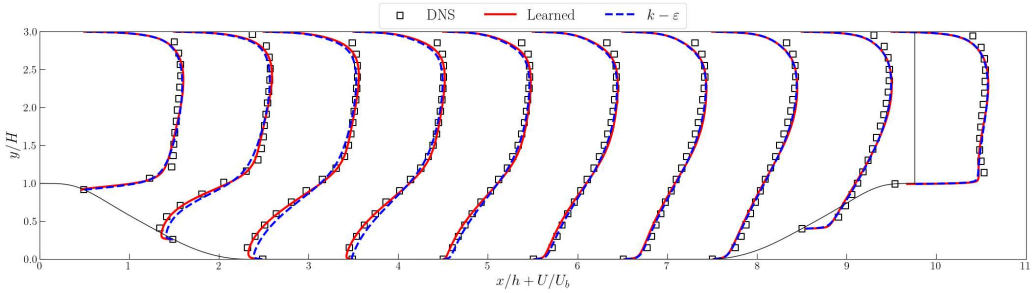

FIG. 19. The non-dimensional streamwise velocity profile obtained by the standard *k-ε* model and the learned model, compared with DNS data. (α=1.2, non-training case)

The results above show that the learned turbulence model significantly improves the prediction accuracy of Reynolds stresses and velocity fields under the training case (α=0.8) and performs well in non-training cases with different geometries (α=1.0 and α=1.2). This indicates that the learned model has a certain degree of generalization capability for large separation turbulence flows with varying geometries.

V. CONCLUSION

In this study, we proposed a novel unit-constrained turbulence modeling framework using symbolic regression to improve the prediction accuracy of LEVMs for large separated turbulence. The proposed framework employs symbolic regression to learn explicit equations between Reynolds stress discrepancies and mean flow features from RANS baseline data and high-fidelity DNS turbulence data. By incorporating the obtained equations as correction terms into the constitutive equations, a new learned turbulence model is obtained. Unit consistency constraints are applied during the symbolic regression to enhance physical realizability.

To validate the effectiveness of the proposed turbulence modeling framework, the flow over periodic hills is used as training and testing case. The findings reveal that the proposed framework exhibits superior modeling performance for large separated turbulence compared to the standard *k-ε* model. In the training case, the learned turbulence model significantly improves the accuracy of Reynolds stress predictions compared to the standard *k-ε* model. For the

velocity field, where the learned model's predictions of the size of the separation and recirculation zones are closer to the DNS results, and the velocity distribution within the recirculation zones at different streamwise positions is more accurate. Even in flows with geometries different from the training case, the learned model demonstrates superior performance, indicating a certain degree of generalization capability.

Future efforts will aim to broaden the training dataset to include a wider variety of flow types, thereby extending the model's applicability to more complex turbulent flows. The goal is to develop a universal turbulence model capable of accurately predicting flows involving complex turbulent phenomena such as shock-boundary layer interactions and transition. Additionally, the Reynolds stress discrepancies obtained through symbolic regression in this study are algebraic functions of the mean flow features, meaning they are determined solely by local quantities. However, Reynolds stresses may also be influenced by the transport of non-local flow quantities. Future work could incorporate differential operators into the symbolic regression to establish transport equations, thereby accounting for the influence of non-local quantities on Reynolds stresses.

CONFLICT OF INTEREST

The authors have no conflicts to disclose.

DATA AVAILABILITY

The data that support the findings of this study are available from the corresponding author upon reasonable request.

Appendix A: Geometry of the parametric periodic hills

The geometry of the first hill upstream in the periodic hills (α=1.0) is given by the following equation[26]:

$$\begin{cases} \hat{y} = \min\left(1;1+2.42\times10^{-4}\hat{x}^2-7.588\times10^{-5}\hat{x}^3\right) & ,\hat{x}\in[0,0.3214] \\ \hat{y} = 0.8955+3.484\times10^{-2}\hat{x}-3.629\times10^{-3}\hat{x}^2+6.749\times10^{-5}\hat{x}^3 & ,\hat{x}\in(0.3214,0.5] \\ \hat{y} = 0.9213+2.931\times10^{-2}\hat{x}-3.234\times10^{-3}\hat{x}^2+5.809\times10^{-5}\hat{x}^3 & ,\hat{x}\in(0.5,0.7143] \\ \hat{y} = 1.445-4.927\times10^{-2}\hat{x}+6.95\times10^{-4}\hat{x}^2-7.394\times10^{-6}\hat{x}^3 & ,\hat{x}\in(0.7143,1.071] \\ \hat{y} = 0.6401+3.123\times10^{-2}\hat{x}-1.988\times10^{-3}\hat{x}^2+2.242\times10^{-5}\hat{x}^3 & ,\hat{x}\in(1.071,1.429] \\ \hat{y} = \max\left(0;2.0139-7.18\times10^{-2}\hat{x}+5.875\times10^{-4}\hat{x}^2+9.553\times10^{-7}\hat{x}^3\right) & ,\hat{x}\in(1.429,1.929] \end{cases} \tag{A1}$$

where $\hat{x}$ and $\hat{y}$ represent the non-dimensional coordinates of the hill, with the expressions given by $\hat{x}=x/H$ and $\hat{y}=y/H$, respectively. The geometry of the second hill downstream is derived by mirroring the first hill along the *y*-axis and then translating it along the *x*-axis.

The relationship between the total length L_x of the domain and the parameter α is as follows:

$$L_x / H = 3.858\alpha + 5.142 \tag{A2}$$

As α changes, L_x also changes accordingly, and the shape of the hills and the bottom wall will be stretched along the x-axis to accommodate the variation in L_x.

REFERENCES

[1] P.A. Durbin, "Some Recent Developments in Turbulence Closure Modeling," Annu. Rev. Fluid Mech. **50**, 77–103 (2018).

[2] J.-X. Wang, J.-L. Wu, and H. Xiao, "Physics-informed machine learning approach for reconstructing Reynolds stress modeling discrepancies based on DNS data," Phys. Rev. Fluids **2**, 034603 (2017).

[3] T.B. Gatski, and T. Jongen, "Nonlinear eddy viscosity and algebraic stress models for solving complex turbulent flows," Prog. Aerosp. Sci. **36**, 655–682 (2000).

[4] S.B. Pope, *Turbulent Flows* (Cambridge University Press, 2000).

[5] D.C. Wilcox, *Turbulence Modeling for CFD* (DCW industries, 1998).

[6] J. Wu, H. Xiao, R. Sun, and Q. Wang, "Reynolds-averaged Navier–Stokes equations with explicit data-driven Reynolds stress closure can be ill-conditioned," J. Fluid Mech. **869**, 553–586 (2019).

[7] K. Duraisamy, Z.J. Zhang, and A.P. Singh, "New approaches in turbulence and transition modeling using data-driven techniques," in *53rd AIAA Aerospace Sciences Meeting*, (2015), p. 1284.

[8] E.J. Parish, and K. Duraisamy, "A paradigm for data-driven predictive modeling using field inversion and machine learning," J. Comput. Phys. **305**, 758–774 (2016).

[9] J. Ling, A. Kurzawski, and J. Templeton, "Reynolds averaged turbulence modelling using deep neural networks with embedded invariance," J. Fluid Mech. **807**, 155–166 (2016).

[10] J.-L. Wu, H. Xiao, and E. Paterson, "Physics-informed machine learning approach for augmenting turbulence models: A comprehensive framework," Phys. Rev. Fluids **3**, 074602 (2018).

[11] X. Shan, Y. Liu, W. Cao, X. Sun, and W. Zhang, "Turbulence Modeling via Data Assimilation and Machine Learning for Separated Flows over Airfoils," AIAA J. **61**, 3883–3899 (2023).

[12] K. Duraisamy, G. Iaccarino, and H. Xiao, "Turbulence Modeling in the Age of Data," Annu. Rev. Fluid Mech. **51**, 357–377 (2019).

[13] Y. Zhao, H.D. Akolekar, J. Weatheritt, V. Michelassi, and R.D. Sandberg, "RANS turbulence model development using CFD-driven machine learning," J. Comput. Phys. **411**, 109413 (2020).

[14] M. Schmelzer, R.P. Dwight, and P. Cinnella, "Discovery of Algebraic Reynolds-Stress Models Using Sparse Symbolic Regression," Flow Turbul. Combust. **104**, 579–603 (2020).

[15] H. Tang, Y. Wang, T. Wang, and L. Tian, "Discovering explicit Reynolds-averaged turbulence closures for turbulent separated flows through deep learning-based symbolic regression with non-linear corrections," Phys. Fluids **35**, 025118 (2023).

[16] C. Wu, and Y. Zhang, "Enhancing the shear-stress-transport turbulence model with symbolic regression: A generalizable and interpretable data-driven approach," Phys. Rev. Fluids **8**, (2023).

[17] M. Wu, W. Li, L. Yu, L. Sun, J. Liu, and W. Li, "Discovering Mathematical Expressions Through DeepSymNet: A Classification-Based Symbolic Regression Framework," IEEE Trans. Neural Netw. Learning Syst., 1–15 (2023).

[18] W. Tenachi, R. Ibata, and F.I. Diakogiannis, "Deep Symbolic Regression for Physics Guided by Units Constraints: Toward the Automated Discovery of Physical Laws," Astrophys. J. **959**, (2023).

[19] P. Spalart, and S. Allmaras, "A one-equation turbulence model for aerodynamic flows," in *30th Aerospace Sciences Meeting and Exhibit*, (AIAA, 1992).

[20] B.E. Launder, and D.B. Spalding, "The numerical computation of turbulent flows," Comput. Method Appl. Mech. Eng. **3**, 269–289 (1974).

[21] D. Wilcox, "Reassessment of the Scale-Determining Equation for Advanced Turbulence Models," AIAA J. **26**, 1299–1310 (1988).

[22] F.R. Menter, "Two-equation eddy-viscosity turbulence models for engineering applications," AIAA J. **32**, 1598–1605 (1994).

[23] M. Schmidt, and H. Lipson, "Distilling Free-Form Natural Laws from Experimental Data," Science **324**, 81–85 (2009).

[24] S.-M. Udrescu, and M. Tegmark, "AI Feynman: A physics-inspired method for symbolic regression," Sci. Adv. **6**, (2020).

[25] B.K. Petersen, M. Landajuela, T.N. Mundhenk, C.P. Santiago, S.K. Kim, and J.T. Kim, "Deep symbolic regression: Recovering mathematical expressions from data via risk-seeking policy gradients," arXiv:1912.04871 (2021).

[26] H. Xiao, J.-L. Wu, S. Laizet, and L. Duan, "Flows over periodic hills of parameterized geometries: A dataset for data-driven turbulence modeling from direct simulations," Comput. Fluids **200**, 104431 (2020).

[27] H. Xiao, J.-L. Wu, J.-X. Wang, R. Sun, and C.J. Roy, "Quantifying and Reducing Model-Form Uncertainties in Reynolds-Averaged Navier-Stokes Simulations: A Data-Driven, Physics-Based Bayesian Approach," J. Comput. Phys. **324**, 115–136 (2016).